Theoretical Analysis of Thermal Transport in Graphene Supported on Hexagonal Boron Nitride: The Importance of Strong Adhesion Due to π-Bond Polarization

Alexander J. Pak and Gyeong S. Hwang*

McKetta Department of Chemical Engineering, University of Texas, Austin, Texas 78712, USA

(Received 14 May 2016; revised manuscript received 4 August 2016; published 26 September 2016)

One important attribute of graphene that makes it attractive for high-performance electronics is its inherently large thermal conductivity (κ) for the purposes of thermal management. Using a combined density-functional theory and classical molecular-dynamics approach, we predict that the κ of graphene supported on hexagonal boron nitride (h-BN) can be as large as 90% of the κ of suspended graphene, in contrast to the significant suppression of κ (more than 70% reduction) on amorphous silica. Interestingly, we find that this enhanced thermal transport is largely attributed to increased lifetimes of the in-plane acoustic phonon modes, which is a notable contrast from the dominant contribution of out-of-plane acoustic modes in suspended graphene. This behavior is possible due to the charge polarization throughout graphene that induces strong interlayer adhesion between graphene and h-BN. These findings highlight the potential benefit of layered dielectric substrates such as h-BN for graphene-based thermal management, in addition to their electronic advantages. Furthermore, our study brings attention to the importance of understanding the interlayer interactions of graphene with layered dielectric materials which may offer an alternative technological platform for substrates in electronics.

DOI: 10.1103/PhysRevApplied.6.034015

I. INTRODUCTION

Because of its large electrical and thermal conductivity, graphene has been extensively explored as an active channel material in nanoscale and flexible electronics [1]. In this context, these two-dimensional sheets are typically supported on or encased in electrically insulating substrates. Recently, few-layer hexagonal boron nitride (h-BN) has been tested for its suitability as a dielectric substrate; the small lattice mismatch and atomically smooth surface of h-BN results in carrier mobilities that are an order of magnitude larger than that of conventional SiO_2 substrates [2]. Few-layer h-BN stacks have also been proposed as a means to improve heat management, thereby mitigating degradation of the substrate from local heating and enhancing overall device performance [3]. Ideally, such vertically stacked van der Waals (VDW) heterostructures can be used to maximize the thermal anisotropy by promoting basal (i.e., in-plane) thermal conductivity (κ) while minimizing the interfacial (i.e., cross-plane) thermal conductance (G). To achieve this goal, it is imperative to explore the fundamental mechanisms of both in-plane and cross-plane thermal transport at these interfaces. However, only a limited number of experimental [4] and theoretical [5,6] studies have reported on the thermal transport at graphene and h-BN interfaces with their primary focus on G.

To investigate the κ and G of supported graphene, we advocate the use of molecular simulations to develop atomic-level insights. The increasingly powerful capabilities of classical molecular-dynamics (MD) simulations have encouraged their use for interfacial thermal transport investigations. While much of the earlier theoretical work that focused on understanding the thermal transport physics of graphene relied on first-principles calculations based on density-functional theory (DFT) [7,8], the use of classical force fields has recently been demonstrated to reproduce comparable results with experimental data [9,10]. These force fields enable the direct calculation of κ and G from MD simulations which can also implicitly incorporate temperature-dependent and full anharmonicity [11]. MD simulations are also useful for the study of disordered systems such as graphene supported on amorphous SiO_2 (a-SiO_2), which require system sizes that are computationally burdensome for DFT-based calculations. For example, a recent study by our group revealed that the κ of (a-SiO_2)-supported graphene tends to scale directly with the contact force distribution (i.e., the variance of the VDW forces), which is sensitive to the morphology at the interface [12]. Therefore, these simulations must incorporate accurate representations of the interfacial energetics.

A central aspect of layered materials is the combination of dispersion forces, electrostatic interactions, and Pauli repulsions that dictate the interlayer interactions [13]. The case of graphene supported on h-BN is particularly interesting as the polar nature of the B—N bond can induce electronic polarization throughout the graphene sheet [14,15]. Therefore, the framework of this work is as

*Author to whom all correspondence should be addressed.
gshwang@che.utexas.edu

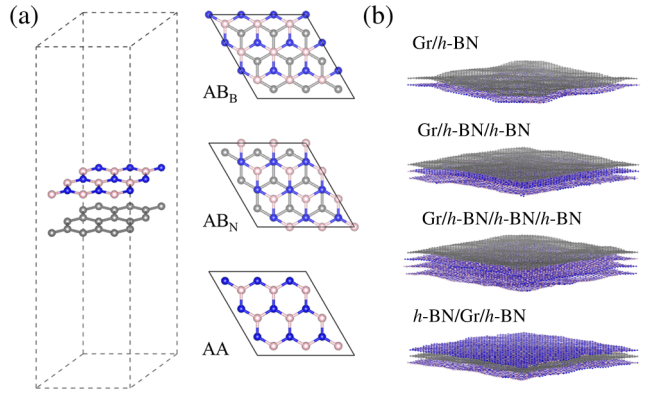

FIG. 1. (a) Schematic of the simulation cell used in DFT calculations and representations of the three stacking orientations. (b) Schematic of the graphene (Gr) and hexagonal boron nitride (h-BN) heterostructures used in MD simulations. Gray, pink, and blue balls represent C, B, and N atoms, respectively.

follows. We first investigate the nature of the graphene/h-BN interfacial interactions using dispersion-corrected DFT (DFT D2). We then explore the κ and G of various graphene/h-BN heterostructures, as shown in Fig. 1, based on MD simulations using the Mie potential with parameters we optimize. Our results show that the κ (and G) of supported graphene can be enhanced (diminished) by increasing the number of h-BN support layers. Our analysis attributes this behavior to the reduced strain within graphene and increased in-plane phonon lifetimes, which is possible due to the strong interlayer adhesion between graphene and h-BN. These findings highlight the possibility of significantly improving the thermal conductivity of graphene and may prove useful for the study of other layered materials.

II. INTERLAYER INTERACTIONS BETWEEN GRAPHENE AND h-BN

We first investigate the nature of the interlayer interactions between monolayer graphene and h-BN using VDW-corrected DFT calculations. As shown in Fig. 1(a), we consider three possible stacking configurations: AB$_B$, AB$_N$, and AA; in the former two cases, the subscript denotes the h-BN sublattice that is eclipsed by C, while in the last case, both sublattices are eclipsed.

The charge-density difference plots in Fig. 2 show that in each case, the two C sublattices experience a noticeable charge redistribution as a result of interactions with the B and N sublattices. Previous studies [14,16] have shown that the so-called symmetry breaking resulting from sublattice polarization is responsible for the observed band-gap opening in supported graphene. We focus on the AB$_B$ orientation shown in Fig. 2(a), as this is the most energetically favorable configuration (as discussed below). Our DFT D2 calculations reveal that the C sublattice directly adjacent to the B sublattice tends to accumulate electron

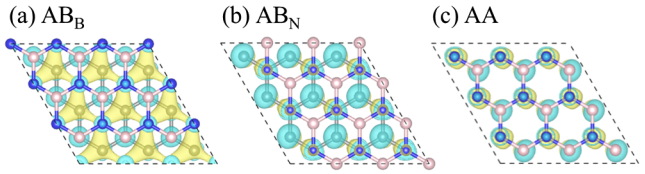

FIG. 2. Charge-density difference plots for monolayer h-BN/graphene for (a) AB$_B$, (b) AB$_N$, and (c) AA stacking orientations. The pink, blue, and gray balls denote B, N, and C atoms, respectively. The yellow (blue) shaded regions depict isosurfaces with positive (negative) charge at a value of 0.0002 e/bohr^3. Energetically optimal separation distances between h-BN and graphene are used in each case (around 3.1, 3.3, and 3.4 Å, respectively).

density. On the other hand, the C sublattice that is staggered with the N sublattice exhibits laterally broadened electron depletion. With this polarization of the graphene π system, the optimal separation distance from h-BN is 3.1 Å. However, in the AB$_N$ [Fig. 2(b)] and AA [Fig. 2(c)] configurations, the electron density tends to be vertically polarized rather than laterally broadened, while the predicted separation distances are 3.3 and 3.4 Å, respectively. Upon the addition of a second h-BN layer, our calculations (Ref. [17] Fig. S1) show that the charge-density redistribution throughout graphene remains qualitatively the same as in Fig. 2, which suggests that increasing the number of h-BN layers does not noticeably affect the polarization of graphene.

Next, we compute the interfacial binding energy (E_b) using DFT D2 as presented in Fig. 3 (see Sec. V). In the AB$_B$ configuration, E_b can be as large as 23.4 meV/Å^2, which is comparatively larger than that of bilayer graphene (18.7 meV/Å^2 using DFT D2). Another insightful comparison is to that of graphene on Cu(111), a substrate commonly used for CVD growth of graphene, which has

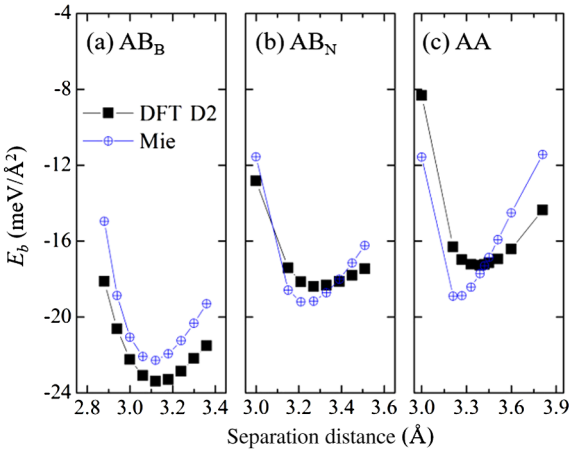

FIG. 3. Comparison of the computed interlayer binding energy (E_b) at varying interlayer distances for (a) AB$_B$, (b) AB$_N$, and (c) AA orientations using DFT D2 (black squares) and optimized Mie parameters from this work (blue open circles).

an experimentally measured adhesion energy of 30–32 meV/Å^2 [18,19] and a DFT D2 calculated E_b of 30.1 meV/Å^2. The large adhesion energy between graphene and Cu is likely attributed to a charge-transfer-induced short-range electrostatic interaction, while the graphene p_z and Cu d_{z2} orbitals exhibit weak coupling [20]. Similarly, the combination of charge polarization and lattice matching between the graphene and *h*-BN sheets can result in a larger E_b with respect to bilayer graphene. We should also note that E_b is strongly orientation dependent and can reduce by up to 40% in the AA or AB_N configurations. However, previous theoretical results [21,22] on graphene and *h*-BN bilayers have found that the sliding barrier between orientations is at least an order of magnitude smaller than the estimated E_b. Therefore, upon thermal annealing, we can expect the graphene sheet to slide into the most favorable AB_B configuration. Another interesting comparison is to that of bilayer *h*-BN. In the AA' configuration in which B of the first layer is adjacent to N of the second layer, the predicted E_b is 24.1 meV/Å^2. This is marginally stronger than that of the graphene/*h*-BN interface, which we can expect as the interlayer B and N atoms have correspondingly stronger electrostatic attractions.

To describe E_b, we adopt the Mie potential (see Sec. V) and optimize the parameters in order to agree with our DFT D2 results (Fig. 3); the optimized parameters can be found in Table I. The Mie potential is a generalized Lennard Jones (LJ) potential that allows for fine-tuning of the interatomic attractive and repulsive contributions using the following equation:

$$E_b = \sum_{i,j>i} \left(\frac{n_{\mathrm{rep}}}{n_{\mathrm{rep}} - n_{\mathrm{att}}}\right) \left(\frac{n_{\mathrm{rep}}}{n_{\mathrm{att}}}\right)^{\left(\frac{n_{\mathrm{att}}}{n_{\mathrm{rep}} - n_{\mathrm{att}}}\right)} \varepsilon \times \left[\left(\frac{\sigma}{r_{ij}}\right)^{n_{\mathrm{rep}}} - \left(\frac{\sigma}{r_{ij}}\right)^{n_{\mathrm{att}}}\right], \quad (1)$$

where ε is the well depth, σ is the zero-energy distance, r_{ij} is the distance between atoms i and j, n_{rep} is the exponent of the repulsive term, and n_{att} is the exponent of the attractive term. Note that when $n_{\mathrm{rep}} = 12$ and $n_{\mathrm{att}} = 6$, the Mie potential reduces to the 12-6 LJ potential; however, we find that the 12-6 LJ potential does not suitably describe the energetics that distinguish the three stacking orientations (see Ref. [17] Fig. S2). Herein, we use our optimized Mie parameters to describe the graphene/*h*-BN interlayer interactions. The intralayer interactions for graphene and *h*-BN are described using optimized Tersoff potentials from Refs. [9] and [23], respectively, while the *h*-BN/*h*-BN interlayer interactions are described using a LJ potential from Ref. [24]; the π-bond polarization tends to minimally affect the interatomic forces acting on each atom in graphene (see Ref. [17] Fig. S3). In the next section, we investigate the structure and thermal transport behavior of graphene at the heterostructure interface using classical MD simulations as described below.

TABLE I. Optimized Mie parameters fit to DFT D2 calculations to describe the Gr/*h*-BN interlayer interaction energy.

	ε (meV)	σ (Å)	n_{rep}	n_{att}
C—B	3.6	2.2132	10.38	3.58
C—N	9.0	3.2222	14.85	9.84

III. INTERFACIAL STRUCTURE AND ENERGETICS

We consider four cases, as depicted in Fig. 1(b), in which graphene is supported on monolayer *h*-BN, bilayer *h*-BN, trilayer *h*-BN, and encapsulated between two *h*-BN monolayers, hereafter denoted as Gr/*h*-BN, Gr/*h*-BN/*h*-BN, Gr/*h*-BN/*h*-BN/*h*-BN, and *h*-BN/Gr/*h*-BN, respectively.

First, it is informative to gauge the change in the sheet corrugation, which is defined as the standard deviation of the atomic height distribution (σ_h), with different *h*-BN heterostructures. As seen in Table II, σ_h(Gr) and σ_h(*h*-BN) are nearly identical as the graphene sheet tends to be well conformed to the *h*-BN sheet due to the similarity of their lattice constants. Note that in every case, σ_h(Gr) is found to be consistently smaller than σ_h(*h*-BN) since graphene sheets tend to have larger flexural rigidity [25]. As the number of *h*-BN support layers increases, both σ_h(Gr) and σ_h(*h*-BN) are increasingly reduced. This is possible since the additional *h*-BN layers suppress the fluctuations throughout the *h*-BN stack due to the strong *h*-BN/*h*-BN interlayer interaction, which subsequently promotes a flatter graphene sheet. Interestingly, the C—B and C—N pair distribution functions (see Ref. [17] Fig. S4) reveal that the suppression in corrugation is commensurate with the graphene/*h*-BN stacking adopting a more AB_B-like configuration. Likewise, the *h*-BN layers adopt a more AA'-like configuration with the addition of layers.

The sheet corrugation provides valuable insight into the distribution of the atomic forces throughout the graphene sheet, which, in turn, can provide insight into the thermal transport behavior. In this case, we consider the standard deviation of the adhesion force ($\sigma|f_{\mathrm{ad}}|$), which results from the graphene/*h*-BN interlayer interactions and the standard

TABLE II. Average corrugation of graphene or adjacent *h*-BN [σ_h(Gr)/σ_h(*h*-BN)] sheets, the standard deviation of the graphene internal strain force ($\sigma|f_{\mathrm{st}}|$), and interfacial adhesion force ($\sigma|f_{\mathrm{ad}}|$).

	σ_h(Gr)/σ_h(*h*-BN) (Å)	$\sigma\lvert f_{\mathrm{st}}\rvert$ (meV/Å)	$\sigma\lvert f_{\mathrm{ad}}\rvert$ (meV/Å)	Sum
Gr/*h*-BN	0.456/0.459	20.1	26.9	47.0
Gr/*h*-BN/*h*-BN	0.451/0.453	18.6	27.1	45.7
Gr/*h*-BN/*h*-BN/*h*-BN	0.355/0.357	14.6	27.0	41.6
h-BN/Gr/*h*-BN	0.304/0.309	6.6	43.9	50.5

deviation of the strain force throughout graphene ($\sigma|f_{st}|$), which is driven by the C—C bonding forces. Table II shows that the $\sigma|f_{ad}|$ is not particularly sensitive to the small reduction in sheet corrugation, as the already excellent lattice registry does not significantly change upon the addition of h-BN layers. Recall that the excellent lattice registry is possible due to the polarization-driven interlayer adhesion between graphene and h-BN. However, $\sigma|f_{ad}|$ does increase by 60% once graphene is encapsulated between monolayer h-BN sheets (i.e., the h-BN/Gr/h-BN case) as the interlayer interactions now influence both sides. On the other hand, $\sigma|f_{st}|$ is computed to decrease with the number of h-BN layers (and encapsulation), which is consistent with the graphene sheet becoming increasingly flat [i.e., smaller σ_h(Gr)]. Combining the two contributions, we estimate that the overall variation of the force distribution increases with the following trend: Gr/h-BN/h-BN/h-BN < Gr/h-BN/h-BN < Gr/h-BN < h-BN/Gr/h-BN.

IV. ANISOTROPIC THERMAL TRANSPORT

In this section, we investigate the relationship between the interfacial structure and the in-plane κ and cross-plane thermal conductance (G) of graphene supported on h-BN at 300 K using reverse nonequilibrium MD and the thermal-relaxation method, respectively (see Sec. V).

To establish a basis for comparison, we first calculate the κ of free-standing graphene. Given that the distance between the simulated heat source and sink ($L_{\Delta SS}$) is less than the experimentally estimated mean free path of graphene ($l_{MFP} \sim 775$ nm) [26], it is necessary to account for possible phonon boundary scattering in our prediction of κ using the following model based on the 1D kinetic theory of lattices and Matthiessen's rule:

$$\kappa = C_v \nu_p l_{\text{eff}}, \tag{2}$$

$$l_{\text{eff}} = \left(\frac{1}{l_{\text{MFP}}} + \frac{2}{L_{\Delta SS}}\right)^{-1}, \tag{3}$$

$$\frac{1}{\kappa} = \frac{2}{C_v \nu_p} \frac{1}{L_{\Delta SS}} + \frac{1}{C_v \nu_p l_{\text{MFP}}}, \tag{4}$$

where C_v is the constant volume heat capacity (approximately 1.2 MJ m^{-3} K^{-1}) and ν_p is the average phonon group velocity. Note that this model provides some justification for the commonly assumed $\kappa^{-1} \propto L^{-1}$ dependence and offers additional physical meaning to the other constants computed during extrapolation. Using this method, we compute $\kappa = 2295 \pm 212$ W m^{-1} K^{-1} at infinite length. Previous estimations of κ both in simulations and experiments have varied widely between 1000 and 4000 W m^{-1} K^{-1} [7,27–29]. Although the variability of κ in the literature remains a subject of debate, we can use our estimated value to compare the relative influence of the substrate effect due to h-BN layers on κ.

For the cross-plane phonon transport, we similarly compute the G between bilayer graphene sheets as a reference for comparison. Using an effective C_v of 0.61 MJ m^{-3} K^{-1} for two sheets, we find that G is 4.10 ± 1.43 MW m^{-2} K^{-1} (and thermal relaxation time τ is 50 ± 17 ps). This value is comparable to that experimentally measured for the graphene/h-BN interface [4], while it is orders of magnitude lower than that of graphene with metal contacts [30,31].

Figure 4 shows the dependence of κ and G on the heterostructure composition. First, it is clear that κ is reduced to 1818 ± 205 W m^{-1} K^{-1} once supported on monolayer h-BN—a 20% decrease from suspended graphene. The corresponding G is 4.5 ± 0.3 MW m^{-2} K^{-1}, which is comparable to that of bilayer graphene and within the computed standard error. The predicted suppression in κ is noticeably mitigated compared to conventional a-SiO_2 substrates with $\kappa \approx 600$ W m^{-1} K^{-1} [12,32]. The primary difference between the two cases is the exacerbation of $\sigma|f_{ad}|$ in the latter case due to the presence of an atomically rough a-SiO_2 surface to which graphene conforms. We, therefore, attribute the larger κ of Gr/h-BN to the vastly reduced $\sigma|f_{ad}|$ resulting from the graphene sheet conformation to an atomically smooth surface. Interestingly, when we use previously parametrized LJ parameters for graphene and h-BN (which has inherently weaker interlayer binding as shown in Ref. [17] Fig. S2), we compute a larger suppression of κ (see Ref. [17] Fig. S5). This suppression suggests that the polarization-induced strength of the interlayer interactions is necessary to maintain such large values of κ, which we further explore below.

The most interesting feature of Fig. 4 is the predicted enhancement of κ with additional h-BN layers. For example, we compute a κ of 2062 ± 115 W m^{-1} K^{-1} with the

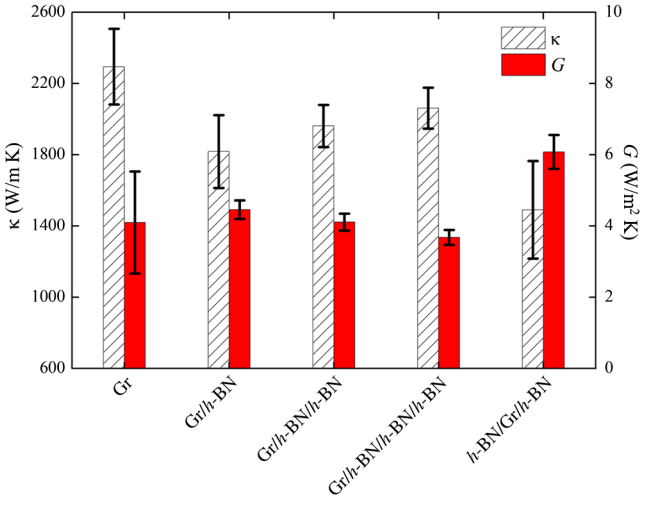

FIG. 4. (a) Thermal conductivity (κ) and thermal conductance (G) of the listed systems at 300 K; the vertical bars represent the standard error.

use of three h-BN layers (Gr/h-BN/h-BN/h-BN), which is only 10% smaller than that of suspended graphene (and 13% larger than that of Gr/h-BN). At the same time, G tends to diminish as the number of h-BN layers increases, which supports previous suggestions [33] that substrate-induced suppressions of κ are proportional to the degree of cross-plane phonon leakage. Furthermore, the final case of encapsulated graphene by h-BN (h-BN/Gr/h-BN) is found to suppress κ to $1491 \pm 274\ \mathrm{W\,m^{-1}\,K^{-1}}$ while G increases to $6.1 \pm 0.5\ \mathrm{MW\,m^{-2}\,K^{-1}}$ (note that this G is effectively double that of a single interface). All of these results are remarkably consistent with the predicted trend in κ following the inverse trend (or direct trend in the case of G) predicted for the variation in forces discussed above. This further supports the hypothesis that reducing the force variation throughout graphene can improve (suppress) the in-plane (cross-plane) thermal transport of supported graphene.

To understand the origins of this behavior, we estimate the effective l_{MFP} of phonons in graphene for each case using the model described in Eq. (4) and depicted in Fig. 5. Using this model, we find that $l_{\mathrm{MFP}} \approx 140$ nm (with $v_p \approx 14$ km/s) in the case of free-standing graphene. Although Ref. [26] approximates an experimental l_{MFP} of 775 nm using a similar model, their reported value is larger because of a significantly larger κ around $4100\ \mathrm{W\,m^{-1}\,K^{-1}}$ and slightly smaller approximate values for C_V and v_p. Nonetheless, our model predicts that the trend in κ directly follows the change in l_{MFP} given that v_p is observed to be nearly constant throughout each case (see Ref. [17] Fig. S6). To confirm that v_p should remain uninfluenced, we compute the phonon dispersion profiles and find that they remain virtually the same in all cases (see Ref. [17] Fig. S7). Therefore, our findings to this point suggest that increasing the variation of forces throughout graphene effectively reduces l_{MFP} and ultimately decreases κ and increases G.

We can further elucidate the phonon transport behavior by approximating the phonon lifetimes of the acoustic modes using the spectral-energy-density method [34]. Here, the normal mode amplitudes are computed from classical MD and, therefore, include the full temperature-dependent anharmonicity. We should note that we are primarily interested in the relative phonon lifetime trends as explicit magnitudes can be inaccurate due to the single-mode approximation [35]. Figure 5 shows the computed phonon lifetimes for the three acoustic modes—the out-of-plane ZA and two in-plane TA and LA modes—at a chosen k point along the Γ-K direction for each heterostructure. Because of the much larger v_p and lifetimes of the acoustic modes compared to the optical modes, an analysis of the acoustic modes is sufficient to qualitatively understand the overall thermal transport behavior. First, in the case of graphene, our calculations predict considerably longer lifetimes for this particular ZA mode (approximately 70 ps) compared to the corresponding LA and TA modes, which is consistent with previous theoretical results that attribute the large κ of suspended graphene to the

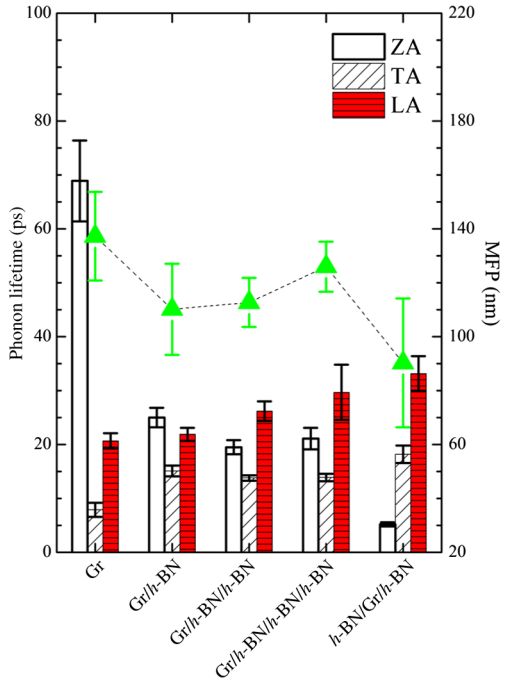

FIG. 5. Comparison between the listed graphene/h-BN heterostructures of the (right) phonon lifetimes for the three acoustic modes at $k = (2/11)(2\pi/a_1, 2\pi/a_2)$ extracted from spectral energy density analysis and (left) effective total mean free path (MFP) of phonons from Eq. (4). The k point is chosen to be close enough to the Brillouin-zone center to sample acoustic branches with high group velocity while being far enough to clearly distinguish the three branches. The up-shift in the phonon mode frequency compared to the graphene case is less than 7% for the ZA branch and less than 2% for the TA and LA branches.

flexural modes [28]. Once supported on monolayer h-BN, the ZA-mode lifetime is estimated to decrease significantly to around 25 ps. In contrast, the lifetimes of the LA and TA modes are predicted to increase. Nonetheless, we can attribute the observed reduction of κ in the Gr/h-BN case to the significant suppression of the ZA-mode lifetime. Interestingly, the addition of h-BN layers has a minimal effect on the ZA-mode lifetimes. However, the lifetimes of the TA and LA modes appear to continuously increase as additional h-BN layers are added; the enhancement of these in-plane modes can explain our observed increase in κ and l_{MFP}. Finally, in the h-BN/Gr/h-BN case, the observed decrease in κ follows from a further substantial reduction in the ZA-mode lifetime despite the enhancement of the TA- and LA-mode lifetimes.

It is quite intuitive to understand the thermal transport with respect to the contributions from the out-of-plane and in-plane phonon modes given the two-dimensional nature of graphene. In Fig. 6, we probe the relationship between the lifetimes of these modes and the standard deviation of the total acting forces per carbon atom in the out-of-plane ($\sigma|f_z|$) and in-plane ($\sigma|f_{xy}|$) directions. Expectedly, our simulations reveal a distinct inverse relationship between

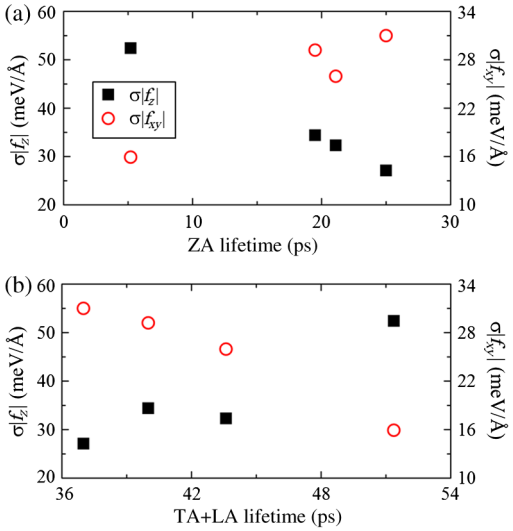

FIG. 6. Comparison between the (a) out-of-plane ZA and (b) combined in-plane TA and LA phonon lifetimes to the variance of the atomic forces experienced by the graphene sheet in the out-of-plane ($\sigma|f_z|$) and in-plane ($\sigma|f_{xy}|$) directions.

the ZA-mode lifetime and $\sigma|f_z|$, which dramatically increases when graphene is encapsulated by h-BN sheets, while seemingly uninfluenced by $\sigma|f_{xy}|$. Physically, one could imagine that the greater irregularity of the forces perpendicular to graphene disrupt possible collective flexural motions. On the other hand, the LA- and TA-mode lifetimes are inversely dependent upon $\sigma|f_{xy}|$, which decreases as the graphene sheet becomes increasingly flat with additional h-BN support, while seemingly independent of $\sigma|f_z|$; the in-plane vibrational motions become increasingly unhindered as the graphene sheet becomes flatter. This suggests that one possible route to enhance the thermal transport in supported graphene is to minimize the variation of strain throughout the sheet. In a perfectly flat configuration, the in-plane LA and TA modes may completely dominate heat transport, unlike the suspended graphene case in which the thermally induced flexural ripples likely dominate heat transport. As a proof of concept, we consider the κ of graphene supported on and encapsulated in perfectly stiff monolayer h-BN; in the absence of rippling throughout the substrate, graphene can achieve a nearly planar configuration due to the strong interlayer adhesion. We compute κ to be 2436 ± 294 W m^{-1} K^{-1} and 2301 ± 107 W m^{-1} K^{-1}, respectively, which suggests that supported graphene can acquire thermal transport properties comparable to suspended graphene or potentially greater.

V. COMPUTATIONAL METHODS

A. Optimization of interatomic interactions

To study the thermal transport in Gr/h-BN heterostructures, the intra- and interatomic interactions are described using classical force fields within a molecular-dynamics framework. The Tersoff bond-order potential is commonly used in thermal transport simulations when sufficiently parametrized to reproduce the phonon dispersion behavior, especially for acoustic phonon modes near the Brillouin-zone center. Here, the optimized parameters from Lindsay and Broido [9] and Sevik *et al.* [23] are used for the graphene and h-BN sheets, respectively.

The interlayer interactions between graphene and h-BN are optimized to reproduce the energy predicted from semiempirical dispersion-corrected DFT using the method of Grimme [36] (the so-called DFT D2) based on the GGA-PBE functional [37] as implemented in the Vienna *ab initio* simulation package [38]. The projector-augmented-wave method [39] is used to describe the interaction between core and valence electrons with a plane-wave basis set using a kinetic energy cutoff of 450 eV. The training sets are constructed from three different stacking orientations by varying the interlayer separation distance. Here, a lattice constant of $a = 2.488$ Å is used, corresponding to 0.9% tensile (compressive) strain for graphene (h-BN). All training set calculations are performed using a periodic 3×3 hexagonal unit cell with vacuum spacing of 30 Å in the perpendicular direction to avoid interactions with the periodic images; a 6×6 Monkhorst-Pack k-point mesh [40] is used to sample the Brillouin zone. The three stacking orientations are denoted as AA, AB_B, and AB_N in which the subscript denotes the h-BN atom that is eclipsed by the adjacent C atom, as depicted in Fig. 1(a).

The classical Mie potential is optimized to emulate the graphene/h-BN binding energies from DFT D2 through minimization of the cross-validation error objective function (δ):

$$\delta = \sqrt{\frac{1}{N}\sum_{n=1}^{N}(E^n_{\mathrm{DFT\,D2}} - E^n_{\mathrm{Mie}})^2},$$

where $E^n_{\mathrm{DFT\,D2}}$ and E^n_{Mie} refer to the DFT D2 and Mie potential energies, respectively, for the nth of N training sets. The interlayer interactions between the h-BN sheets are described using the LJ potential from Neek-Amal and Peeters [24].

B. In-plane thermal conductivity

To calculate the κ at 300 K, we prepare each graphene/h-BN system with four different lengths ($L = 94.9$, 189.9, 284.8, and 379.8 nm) and width 7.97 nm corresponding to a (220, 440, 660, 880) $\times$ 32 rectangular supercell. Here, we use a lattice constant of 2.492 Å, which is optimized from the graphene Tersoff potential and results in a 0.2% compressive strain for h-BN. Periodic boundary conditions are employed in all three directions with 10 nm of vacuum space included in the vertical direction to ensure no interactions with the periodic image.

To obtain the κ at each L, we perform ten independent reverse nonequilibrium MD simulations [41] with different initial velocity distributions for statistical accuracy. Each system is equilibrated for 500 ps within the canonical (NVT) ensemble using a Nosé-Hoover thermostat [42] with damping factor 1 ps and followed by 1 ns within the microcanonical (NVE) ensemble while imposing a heat flux through graphene with a velocity swap interval of 50 fs. Here, all MD simulations adopt a 0.5-fs time step and are implemented using the LAMMPS package [43]. The temperature profile is extracted every 5 ps, and the κ is computed from the average gradient of the linear region of the profile between the heat source and sink. Since the Debye temperature of graphene is above 2000 K [44], we include the quantum correction factor according to the procedure shown in Ref. [45]. The κ at infinite length is then extrapolated from $1/L$ vs $1/\kappa$ in which the thickness of graphene is assumed to be 0.335 nm (see Ref. [17] Fig. S8). Such treatment is necessary, as the phonon mean free path of free-standing graphene has previously been estimated to be approximately 775 nm [26], which is much larger than the simulation domain.

C. Cross-plane thermal conductance

To calculate G at 300 K, we prepare each graphene/h-BN system using a 115×115 hexagonal supercell, which we extensively test to be large enough to achieve convergence in G. Each system is equilibrated for 100 ps within the NVT ensemble using a Nosé-Hoover thermostat with damping factor 1 ps and 0.5-fs time step. Then, a thermal pulse is applied to graphene (h-BN stack) at 330 K (270 K) for 1 ps using a Nosé-Hooever thermostat with a damping factor 50 fs, followed by 500 ps of thermal relaxation within the NVE ensemble. This initial temperature gradient is found to be sufficient to maintain well-converged statistics. The temperature of each sheet is extracted every 50 fs. The difference in temperature is fit to an exponential and used to compute the thermal relaxation time (see Ref. [17] Fig. S9). All results are averaged over ten independent simulations with different initial velocity distributions. Because of the 2D nature of each material, the interface can be modeled as a lumped capacitor [46] from which G can be approximated by

$$G = \frac{C_{v,\mathrm{eff}}}{\tau},$$

where τ is the thermal relaxation time, and $C_{v,\mathrm{eff}}$ is the effective heat capacity $(=[1/(dC_{v,\mathrm{Gr}}) + 1/(ndC_{v,h\text{-BN}})]^{-1}$ where d is the layer thickness 3.35 Å, and n is the number of h-BN layers). For all heat capacity calculations, the Debye approximation for 2D crystals in the low-temperature limit is found to be reasonable $[C_v = 18(N/V)k_B(T/\Theta)^2 I]$ with the Debye temperature (Θ) of graphene and h-BN assumed to be 2100 and 400 K, respectively.

D. Spectral-energy-density calculations and energetics

To compute the heterostructure energetics or forces and phonon lifetimes, the same 115×115 hexagonal supercells are used after equilibration at 300 K within the NVT ensemble. Forces and atomic velocities are extracted every 10 fs from 1-ns production runs with 0.5-fs time steps. The results for each system are averaged over five independent runs with different initial velocity distributions. The spectral energy density is computed using the procedure described in Ref. [34] at $k = (2/11)(2\pi/a_1, 2\pi/a_2)$, which is chosen to be close enough to the Brillouin-zone center to distinctly sample the acoustic branches while they maintain a large group velocity. The phonon frequency modes are found to up-shift slightly (by 7% for the ZA modes and 2% for the TA and LA modes). Peaks (see Ref. [17] Fig. S10) are fit using Fityk [47].

VI. CONCLUSIONS

In this work, the thermal conductivity (κ) and interfacial thermal conductance (G) of graphene supported with few-layer h-BN sheets (i.e., monolayer, bilayer, trilayer, and encapsulated h-BN) are investigated using a combined DFT and classical MD approach. Using DFT, we first study the nature of the interlayer interactions between graphene and h-BN. Our DFT simulations demonstrate that the h-BN sheets induce sublattice charge polarization along the graphene lattice, which, in turn, promotes strong interfacial adhesion particularly in the optimal AB_B stacking configuration. Because of the deficiencies in the standard 12-6 Lennard Jones potential, the parameters for the Mie potential are optimized to describe the interlayer interactions. MD simulations are then performed to evaluate the κ and G of graphene supported on few-layer h-BN. In transitioning from fully suspended to supported on monolayer h-BN, κ is reduced from around 2300 to 1800 $\mathrm{W\,m^{-1}\,K^{-1}}$, which is still much larger than that of graphene on amorphous SiO_2 ($\cong$600 $\mathrm{W\,m^{-1}\,K^{-1}}$), and G is around 4.5 $\mathrm{MW\,m^{-2}\,K^{-1}}$. Interestingly, κ and the overall thermal transport anisotropy (i.e., κ/G) increase as the number of h-BN support layers increases. Our analysis reveals that the increased thermal conductivity is driven by the enhanced lifetime of the in-plane LA and TA acoustic phonon modes, while the ZA-mode lifetime is suppressed, which, in turn, is possible due to the strong adhesion between graphene and h-BN and the resultant flattening of the sheets in the heterostructure to minimize the fluctuations in the internal strain forces. These findings suggest that one possible route to enhance the thermal transport in supported graphene is to bolster the lifetimes of the in-plane phonon modes by minimizing the local variation of forces throughout the graphene sheet. In fact, our results highlight the potential to go beyond the thermal transport limits of suspended graphene using such a strategy, which

may be ideal for thermal management in nanoelectronic devices.

On a final note, it is evident that much of the physics of phonon transport in layered materials remains unclear. However, the systematic computational framework presented here may be useful for the exploration of other graphene and layered dielectric material heterostructures, in addition to structural factors including polycrystallinity, lattice strain, and Moiré patterns. In particular, the variation of the forces along the graphene sheet can be an intuitive physical descriptor to understand phonon transport. Yet, future investigations of the relative contributions of the in-plane and cross-plane phonon modes may require better descriptions of both the interlayer nonbonding interactions and the bonding forces throughout each sheet. In particular, it may be worthwhile to explore quantum-mechanical descriptions of weak noncovalent interactions that are more rigorous than the semiempirical Grimme corrections to dispersion used here. We anticipate that this work can serve as motivation to develop more robust computational methods to explore in depth the thermal transport of layered-material heterostructures.

ACKNOWLEDGMENTS

This work is supported in part by the Robert A. Welch Foundation (Grant No. F-1535) and the NSF-NASCENT Engineering Research Center (Cooperative Agreement No. EEC-1160494). We would also like to thank the Texas Advanced Computing Center for use of their computing resources.

[1] K. C. Yung, W. M. Wu, M. P. Pierpoint, and F. V. Kusmartsev, Introduction to graphene electronics—A new era of digital transistors and devices, Contemp. Phys. **54**, 233 (2013).

[2] C. R. Dean, A. F. Young, I. Meric, C. Lee, L. Wang, S. Sorgenfrei, K. Watanabe, T. Taniguchi, P. Kim, K. L. Shepard, and J. Hone, Boron nitride substrates for high-quality graphene electronics, Nat. Nanotechnol. **5**, 722 (2010).

[3] J. Lee, H. Y. Chang, T. J. Ha, H. Li, R. S. Ruoff, A. Dodabalapur, and D. Akinwande, High-performance flexible nanoelectronics: 2D atomic channel materials for low-power digital and high-frequency analog devices, Tech. Dig. Int. Electron Devices Meet. 491 (2013).

[4] C. C. Chen, Z. Li, L. Shi, and S. B. Cronin, Thermal interface conductance across a graphene/hexagonal boron nitride heterojunction, Appl. Phys. Lett. **104**, 081908 (2014).

[5] X. Wang, T. Huang, and S. Lu, High performance of the thermal transport in graphene supported on hexagonal boron nitride, Appl. Phys. Express **6**, 075202 (2013).

[6] J. Zhang, Y. Hong, and Y. Yue, Thermal transport across graphene and single layer hexagonal boron nitride, J. Appl. Phys. **117**, 134307 (2015).

[7] B. Kong, S. Paul, M. Nardelli, and K. Kim, First-principles analysis of lattice thermal conductivity in monolayer and bilayer graphene, Phys. Rev. B **80**, 033406 (2009).

[8] N. Mounet and N. Marzari, First-principles determination of the structural, vibrational and thermodynamic properties of diamond, graphite, and derivatives, Phys. Rev. B **71**, 205214 (2005).

[9] L. Lindsay and D. A. Broido, Optimized Tersoff and Brenner empirical potential parameters for lattice dynamics and phonon thermal transport in carbon nanotubes and graphene, Phys. Rev. B **81**, 205441 (2010).

[10] Y. Lee and G. S. Hwang, Force matching-based parameterization of the Stillinger-Weber potential for thermal conduction in silicon, Phys. Rev. B **85**, 125204 (2012).

[11] Y. Wang, A. K. Vallabhaneni, B. Qiu, and X. Ruan, Two-dimensional thermal transport in graphene: A review of numerical modeling studies, Nanoscale Micro. Thermophys. Eng. **18**, 155 (2014).

[12] Y. Lee, A. J. Pak, E. Paek, and G. S. Hwang, Principal Role of Contact Force Distribution in Determining the Thermal Conductivity of Supported Graphene, Phys. Rev. Applied **4**, 014006 (2015).

[13] O. Hod, Graphite and hexagonal boron-nitride have the same interlayer distance. Why?, J. Chem. Theory Comput. **8**, 1360 (2012).

[14] G. Giovannetti, P. Khomyakov, G. Brocks, P. Kelly, and J. van den Brink, Substrate-induced band gap in graphene on hexagonal boron nitride: *Ab initio* density functional calculations, Phys. Rev. B **76**, 073103 (2007).

[15] B. Sachs, T. O. Wehling, M. I. Katsnelson, and A. I. Lichtenstein, Adhesion and electronic structure of graphene on hexagonal boron nitride substrates, Phys. Rev. B **84**, 195414 (2011).

[16] Y. Fan, M. Zhao, Z. Wang, X. Zhang, and H. Zhang, Tunable electronic structures of graphene/boron nitride heterobilayers, Appl. Phys. Lett. **98**, 083103 (2011).

[17] See Supplemental Material at http://link.aps.org/supplemental/10.1103/PhysRevApplied.6.034015 for data that describe the influence of additional *h*-BN layers on polarization, the binding energies, and thermal conductivity using a 12-6 LJ potential, pair distribution functions, phonon group velocities, phonon dispersion profiles, and representative simulation data used to extract thermal conductivity, thermal relaxation times, and phonon-mode-specific lifetimes.

[18] J. Lahiri, T. S. Miller, A. J. Ross, L. Adamska, I. I. Oleynik, and M. Batzill, Graphene growth and stability at nickel surfaces, New J. Phys. **13**, 025001 (2011).

[19] Z. Cao, P. Wang, W. Gao, L. Tao, J. W. Suk, R. S. Ruoff, D. Akinwande, R. Huang, and K. M. Liechti, A blister test for interfacial adhesion of large-scale transferred graphene, Carbon **69**, 390 (2014).

[20] Z. Xu and M. J. Buehler, Interface structure, and mechanics between graphene, and metal substrates: A first-principles study, J. Phys. Condens. Matter **22**, 485301 (2010).

[21] G. Constantinescu, A. Kuc, and T. Heine, Stacking in Bulk and Bilayer Hexagonal Boron Nitride, Phys. Rev. Lett. **111**, 036104 (2013).

[22] W. Gao and A. Tkatchenko, Sliding Mechanisms in Multilayered Hexagonal Boron Nitride and Graphene: The Effects of Directionality, Thickness, and Sliding Constraints, Phys. Rev. Lett. **114**, 096101 (2015).

[23] C. Sevik, A. Kinaci, J. B. Haskins, and T. Çağın, Characterization of thermal transport in low-dimensional boron nitride nanostructures, Phys. Rev. B **84**, 085409 (2011).
[24] M. Neek-Amal and F. M. Peeters, Graphene on boron-nitride: Moiré pattern in the van der Waals energy, Appl. Phys. Lett. **104**, 041909 (2014).
[25] S. K. Singh, M. Neek-Amal, S. Costamagna, and F. M. Peeters, Thermomechanical properties of a single hexagonal boron nitride sheet, Phys. Rev. B **87**, 184106 (2013).
[26] S. Ghosh, I. Calizo, D. Teweldebrhan, E. P. Pokatilov, D. L. Nika, A. A. Balandin, W. Bao, F. Miao, and C. N. Lau, Extremely high thermal conductivity of graphene: Prospects for thermal management applications in nanoelectronic circuits, Appl. Phys. Lett. **92**, 151911 (2008).
[27] W. Cai, A. L. Moore, Y. Zhu, X. Li, S. Chen, L. Shi, and R. S. Ruoff, Thermal transport in suspended and supported monolayer graphene grown by chemical vapor deposition, Nano Lett. **10**, 1645 (2010).
[28] L. Lindsay, D. A. Broido, and N. Mingo, Flexural phonons and thermal transport in graphene, Phys. Rev. B **82**, 115427 (2010).
[29] A. A. Balandin, Thermal properties of graphene and nanostructured carbon materials, Nat. Mater. **10**, 569 (2011).
[30] K. F. Mak, C. H. Lui, and T. F. Heinz, Measurement of the thermal conductance of the graphene/SiO_2 interface, Appl. Phys. Lett. **97**, 221904 (2010).
[31] Y. K. Koh, M. H. Bae, D. G. Cahill, and E. Pop, Heat conduction across monolayer and few-layer graphenes, Nano Lett. **10**, 4363 (2010).
[32] J. H. Seol, I. Jo, A. L. Moore, L. Lindsay, Z. H. Aitken, M. T. Pettes, X. Li, Z. Yao, R. Huang, D. Broido, N. Mingo, R. S. Ruoff, and L. Shi, Two-dimensional phonon transport in supported graphene, Science **328**, 213 (2010).
[33] M. M. Sadeghi, I. Jo, and L. Shi, Phonon-interface scattering in multilayer graphene on an amorphous support, Proc. Natl. Acad. Sci. U.S.A. **110**, 16321 (2013).
[34] J. A. Thomas, J. E. Turney, R. M. Iutzi, C. H. Amon, and A. J. H. McGaughey, Predicting phonon dispersion relations and lifetimes from the spectral energy density, Phys. Rev. B **81**, 94303 (2010).
[35] Y. Lee, A. J. Pak, and G. S. Hwang, What is the thermal conductivity limit of silicon germanium alloys?, Phys. Chem. Chem. Phys. **18**, 19544 (2016).
[36] S. Grimme, Semiempirical GGA-type density functional constructed with a long-range dispersion correction, J. Comput. Chem. **27**, 1787 (2006).
[37] J. P. Perdew, K. Burke, and M. Ernzerhof, Generalized Gradient Approximation Made Simple, Phys. Rev. Lett. **77**, 3865 (1996).
[38] G. Kresse and J. Furthmüller, Efficient iterative schemes for *ab initio* total-energy calculations using a plane-wave basis set, Phys. Rev. B **54**, 11169 (1996).
[39] P. Blöchl, Projector augmented-wave method, Phys. Rev. B **50**, 17953 (1994).
[40] H. J. Monkhorst and J. D. Pack, Special points for Brillouin-zone integrations, Phys. Rev. B **13**, 5188 (1976).
[41] F. Müller-Plathe, A simple nonequilibrium molecular dynamics method for calculating the thermal conductivity, J. Chem. Phys. **106**, 6082 (1997).
[42] W. Hoover, Canonical dynamics: Equilibrium phase-space distributions, Phys. Rev. A **31**, 1695 (1985).
[43] S. Plimpton, Fast parallel algorithms for short-range molecular dynamics, J. Comput. Phys. **117**, 1 (1995).
[44] D. K. Efetov and P. Kim, Controlling Electron-Phonon Interactions in Graphene at Ultrahigh Carrier Densities, Phys. Rev. Lett. **105**, 256805 (2010).
[45] J.-W. Jiang, J. Lan, J.-S. Wang, and B. Li, Isotopic effects on the thermal conductivity of graphene nanoribbons: Localization mechanism, J. Appl. Phys. **107**, 054314 (2010).
[46] C. F. Carlborg, J. Shiomi, and S. Maruyama, Thermal boundary resistance between single-walled carbon nanotubes and surrounding matrices, Phys. Rev. B **78**, 205406 (2008).
[47] M. Wojdyr, FITYK: A general-purpose peak fitting program, J. Appl. Crystallogr. **43**, 1126 (2010).